


Article

Cavitation Erosion of the Austenitic Manganese Layers Deposited by Pulsed Current Electric Arc Welding on Duplex Stainless Steel Substrates

Ion Mitelea ¹, Daniel Mutaşcu ¹, Ion-Dragoş Uţu ¹ , Corneliu Marius Crăciunescu ¹  and Ilare Bordeaşu ^{2,*}

¹ Department of Materials and Fabrication Engineering, Politehnica University Timisoara, Bulevardul Mihai Viteazul nr.1, 300222 Timișoara, Romania; ion.mitelea@upt.ro (I.M.); daniel.mutascu@student.upt.ro (D.M.); dragos.utu@upt.ro (I.-D.U.); corneliu.craciunescu@upt.ro (C.M.C.)

² Department of Mechanical Machines, Equipment and Transports, Politehnica University Timisoara, Bulevardul Mihai Viteazul nr.1, 300222 Timișoara, Romania

* Correspondence: ilare.bordeasu@upt.ro

Abstract: Fe-Mn-Cr-Ni alloys like Citomangan, delivered in the form of powders, tubular wires, and coated electrodes, are intended for welding deposition operations to create wear-resistant layers. Their main characteristic is their high capacity for surface mechanical work-hardening under high shock loads, along with high toughness and wear resistance. In order to increase the resistance to cavitation erosion, hardfacing of Duplex stainless steel X2CrNiMoN22-5-3 with Citomangan alloy was performed using a new welding technique, namely one that uses a universal TIG source adapted for manual welding with a coated electrode in pulsed current. Cavitation tests were conducted in accordance with the requirements of ASTM G32—2016 standard. Comparing the characteristic cavitation erosion parameters of the manganese austenitic layer, deposited by this new welding technique, with those of the reference steel, highlights an 8–11 times increase in its resistance to cavitation erosion. Metallographic investigations by optical microscopy and scanning electron microscopy (SEM), as well as hardness measurements, were carried out to understand the cavitation phenomena.

Keywords: cavitation erosion; hardfacing by welding; duplex stainless steel; manganese austenitic alloy



Citation: Mitelea, I.; Mutaşcu, D.; Uţu, I.-D.; Crăciunescu, C.M.; Bordeaşu, I. Cavitation Erosion of the Austenitic Manganese Layers Deposited by Pulsed Current Electric Arc Welding on Duplex Stainless Steel Substrates. *Crystals* **2024**, *14*, 315. <https://doi.org/10.3390/cryst14040315>

Academic Editors: Daniel Medyński, Grzegorz Lesiuk and Anna Burduk

Received: 6 March 2024

Revised: 21 March 2024

Accepted: 26 March 2024

Published: 28 March 2024



Copyright: © 2024 by the authors. Licensee MDPI, Basel, Switzerland. This article is an open access article distributed under the terms and conditions of the Creative Commons Attribution (CC BY) license (<https://creativecommons.org/licenses/by/4.0/>).

1. Introduction

The word “cavitation” comes from the Latin word “cavus”, meaning cavity [1]. Cavitation is a phenomenon specific to fluid mechanics, occurring whenever there is a drop in static pressure below the vaporization threshold.

It involves the formation and development of voids (cavitation bubbles) in regions with pressures below a critical value (the saturation vapor pressure), which subsequently implode or burst when they reach areas of high pressure [1–3]. These bubbles contain the vapor phase of the liquid with or without dissolved gas. Depending on the hydrodynamic mechanism, implosion or explosion, shock waves and microjets are generated, which can impact the surfaces of objects in the liquid, creating very high impact pressures that exceed the values of compressive and tensile stresses. Measurements conducted in research laboratories with high-performance equipment show that through these collapses, the vapor pressure of water can increase from 1.704 kN/m² at 15 °C to 101.325 kN/m² at 100 °C [4,5].

The phenomenon occurs in numerous machine components, most commonly in the blades and rotors of hydraulic pumps and turbines, as well as in the propellers of maritime and river vessels [6–8]. It depends not only on its type and instability but also on the response of the engineering materials to the energy transmitted. By its nature, it is highly destructive and can lead to the emergence of noise and vibrations, decrease the equipment performance, the need for inspections and preventive maintenance, and increases in maintenance costs, etc. [9–12].

Duplex stainless steels have an equilibrium microstructure of approx. 50% ferrite and 50% austenite. Therefore, they combine the favorable properties of the two constitutive phases (ferrite and austenite), being considered as high-performance materials for mechanical loading and stress corrosion in environments with chlorine ions [13]. In their chemical composition, the main alloying elements are Cr and Mo, which are ferrite formers, and Ni and N, which are austenite formers. The most important areas of use include hydromechanical equipment (vanes and rotors of hydraulic machines, marine and river ship propellers), offshore oil and gas drilling rigs, etc., usually where higher mechanical strength characteristics are required higher than those of standard austenitic steels (X5CrNi18-10 and X2CrNiMo17-12-2). In addition, the high-cost price of nickel has motivated the selection of these alloys (with a lower content of this alloying element) for new applications where they have become competitive. They also have better resistance to stress-cracking corrosion in chloride environments.

However, a series of research has shown that Duplex stainless steels have a considerably lower cavitation erosion resistance than other stainless steels, a phenomenon due to the presence of ferrite and α/γ interfaces (ferrite/austenite) [14–17]. To reduce wear and corrosion phenomena, research efforts in surface engineering are focused on the development of hard coating techniques by welding, thermal spraying, gas nitriding, thermal evaporation, ion implantation, etc. [18].

Carlos Mario Garzón et al. [19] proved that gas nitriding at high temperatures strongly improves the cavitation erosion resistance of Duplex stainless steel, UNS S31803. Compared to the solution heat treatment, the incubation times are 14–20 times longer and the mass losses decrease by 7.6–23.3 times.

Escobar J.D. et al. [20] show that friction stir welding of Duplex stainless steel, UNS S32205, leads to a reduction in cavitation erosion rate and an increase in incubation time. The explanation is based on recrystallization and refinement of the microstructure as well as the modification of elongated α/γ interfaces.

Kwok C.T. et al. [21] investigated the effect of surface melting with a Nd-YAG laser beam on the intergranular corrosion behavior of Duplex stainless steel, UNS S31803. After laser processing, the ferrite phase δ becomes the primary phase, and the δ/γ equilibrium is disturbed, while the σ phase is eliminated. As a result of carbide or σ phase dissolution, chromium depletion at grain boundaries is reduced, leading to increased resistance to intergranular corrosion.

In order to extend the application of Duplex stainless steel to parts that work in hydrodynamic regimes with strong erosion, such as cavitation, this paper studies the erosion cavitation behavior of manganese austenitic alloys deposited layers on the surface of such steel through a new technological variant of welding hardfacing technology. These iron-based alloys, called “Citomangan”, are frequently used as filler materials delivered in the form of coated electrodes and possess excellent wear and corrosion resistance properties. Along with iron, they contain alloying elements such as Mn, Cr, and Ni in their chemical composition. The research interest in these alloys stems from their recommendation for use in heavy welding loads for valves, shafts, and other components in the automotive, aerospace, oil and gas, metallurgical, and power generation equipment industries, etc.

According to the authors’ knowledge, there are no reports in the literature regarding the cavitation erosion resistance of such coatings deposited using a new welding technique.

2. Materials, Experimental Procedure

The selected material for the substrate is a Duplex stainless steel 2205, symbolized as X2CrNiMoN22-5-3. Its chemical composition (Table 1) was determined through optical emission spectrometry using Thermo Arl QuantoDesk equipment (Thermo Fisher Scientific, Burladingen, Germany).

Before the hardfacing process, the substrate was subjected to a solution heat treatment at a temperature of 1060 °C with rapid quenching in water. The resulting microstruc-

ture consists of austenite, ferrite, and particles of chemical combinations that remained undissolved during heating (see Figure 1).

Table 1. The chemical composition of the material used as the substrate.

Carbon (C)	0.021%
Silicon (Si)	0.79%
Manganese (Mn)	0.82%
Phosphorous (P)	0.019%
Sulfur (S)	0.012%
Chromium (Cr)	22.34%
Nickel (Ni)	5.61%
Molybdenum (Mo)	3.1%
Nitrogen (N)	0.14%
Iron (Fe)	Balance

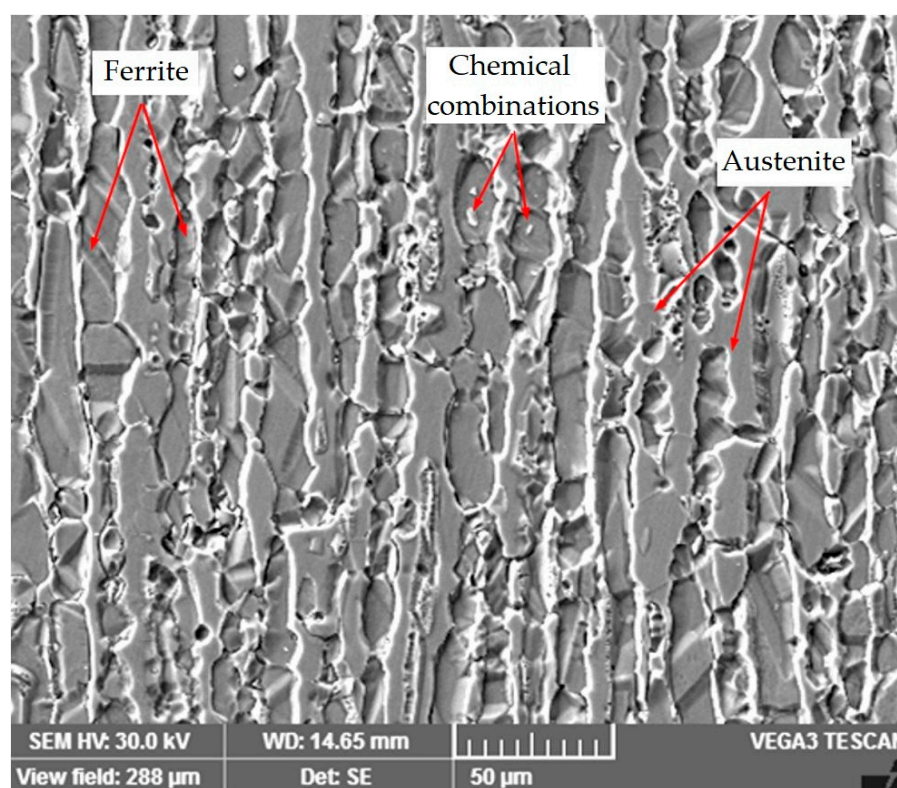


Figure 1. Microstructure of the base metal.

Using a universal welding source, the MAGIC WAVE 300 from Fronius, Wels, Austria which is suitable for manual welding with coated electrode in pulsed current mode, deposits of 1, 2, or 3 layers of austenitic manganese steel (electrode) were made on the considered steel substrates. The novelty lies in the fact that instead of the non-consumable tungsten electrode typically used in the TIG welding torch, the coated electrode selected for hardfacing was fixed in its grip. The average thickness of the first deposited layer was approximately 2.2 mm; after the second layer, the thickness was about 3.6 mm; and for the three layers, it was approximately 5 mm.

Through preliminary tests, the optimal conditions for carrying out the pulsed current welding process have been established.

- basic-coated electrode: CITOMANGAN;
- electrode diameter: 3.25 mm;
- polarity: cc⁺;

- pulse current, I_p : 180 A;
- base current, I_b : 90 A ($50\%I_p$);
- mean (average) current, I_m : 135 A;
- arc voltage, U : 22 V;
- pulse frequency, $f = 1/t_c = 5$ Hz;
- cycle time, $t_c = 1/f = 1/5 = 0.2$ s;
- pulse time, $t_p = 0.5 t_c = 0.1$ s;
- base time, $t_b = 0.5 t_c = 0.1$ s ($t_p = t_b$);
- arc length, $l_a = 3.0$ mm;
- welding speed, $v = 27\text{--}28$ cm/min.

The cavitation tests were conducted on a vibrating device with piezoceramic crystals (Figure 2) made in accordance with the requirements of the ASTM G32-2016 norms [22] and conducted with the computer in which software is implemented that ensures the control of maintaining within the tolerance gap of the parameters that dictate the intensity of the cavitation regime (amplitude and vibration frequency, electronic ultrasound generator power, water temperature) [23].

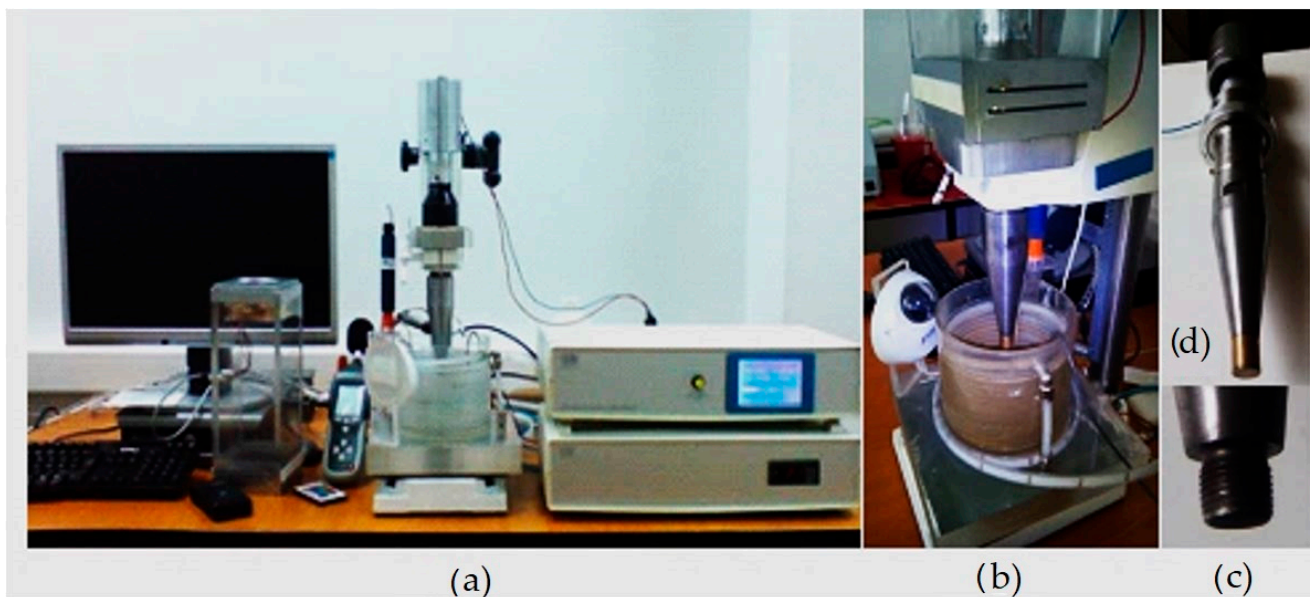


Figure 2. The standard vibrating device with piezoceramic crystals: (a)—general image; (b)—image during the cavitation attack; (c)—the head of the sonotrode in which the cavitation sample is fixed; (d)—the vibrating mechanical system with the sample fixed in the sonotrode.

The functional parameters of the device are as follows:

- power of the ultrasonic electronic generator: 500 W
- frequency of vibrations: $20,000 \pm 2\%$ Hz
- amplitude of vibrations: $50 \mu\text{m}$
- diameter of the sample: 15.8 ± 0.05 mm
- supply voltage: 220 V/50 Hz
- working fluid: tap water, with a temperature of 22 ± 1 °C.

The experiments aimed at determining the cavitation erosion resistance were conducted on sets of 3 samples obtained by machining from the welded pulse current assemblies. The geometric shape of the samples is shown in Figure 3. Before the erosion attack, the exposed cavitation surface was polished to a roughness $R_a = 0.2 \mu\text{m}$.

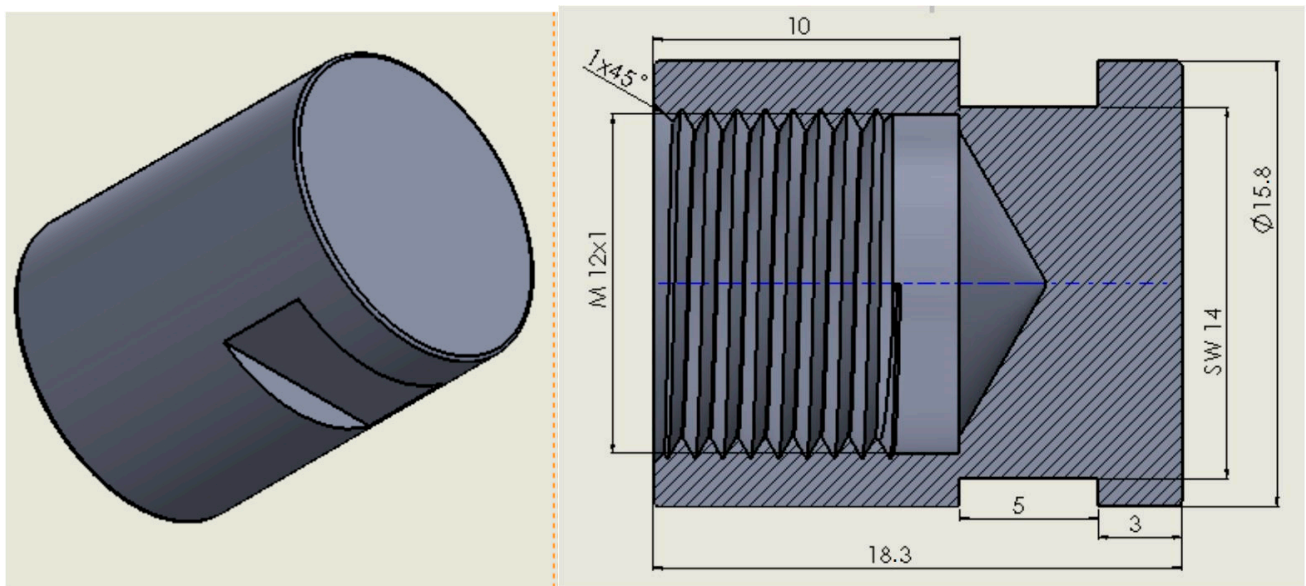


Figure 3. Geometry of the samples exposed to cavitation. The blue dashed line is the symmetry axis of the sample.

The corrosive chemical effect of water on the eroded structure is eliminated through measures included in the experimental procedure and by storing the samples in a desiccator during the stagnation period.

The total testing duration for each sample was 165 min, divided into 12 periods (each consisting of one 5 min period, one 10 min period, and the following 10 periods of 15 min each). At the end of each testing period, the sample was cleaned with acetone, dried with compressed air, and weighed first on an electronic balance and then on an analytical precision balance, type Zatkłady Mechaniki Precyzyjnej WP 1 (Gdańsk, Poland), with a sensitivity of 10^{-5} g.

Subsequently, cross-sections of the deposited layers were taken and their metallographic preparation was carried out through grinding, polishing, and chemical attack operations. Grinding was performed up to SiC-P2500 paper (Schmitz-Metallographie GmbH, Herzogenrath, Germany), polishing up to $0.25\ \mu\text{m}$ with diamond paste, and chemical etching was carried out using Vilella reagent (10 g cupric chloride, 30 mL HCl, and 120 mL distilled water).

The microstructural characterization of the cross-sections was conducted through optical microscopy (Leica DM2700M optical microscope, Leica Mikrosysteme Vertrieb GmbH, Wetzlar, Germany) and scanning electron microscopy (TESCAN VEGA 3 LMU scanning electron microscope with Bruker EDX Quantax from Bruker, Billerica, MA, USA).

Vickers macrohardness (on the Zwick/Roell YHV-S apparatus, ZwickRoell, Ulm, Germany) with an applied force of 5 kgf (HV5) was determined based on measurements recorded across the surfaces of the deposited layers and the base metal, which were ground with SiC-P4000, with a distance of 1.0 mm between each penetration depth and a dwell time of 10 s.

3. Experimental Results

3.1. Hardness Measurements

Figure 4 shows the histogram of the hardness values of the surface hardened by welding with one, two, and three layers, as well as of the substrate material, heat solution treated. It is noted that due to the dilution of the layer with the substrate, the hardness of the surface of the first deposited layer has values of 300–360 HV5, and the surface of the following layers, unaffected by the dilution, varies between 465 HV5 and 490 HV5. According to the reference material, the hardness values are between 260 HV5 and 280 HV5.

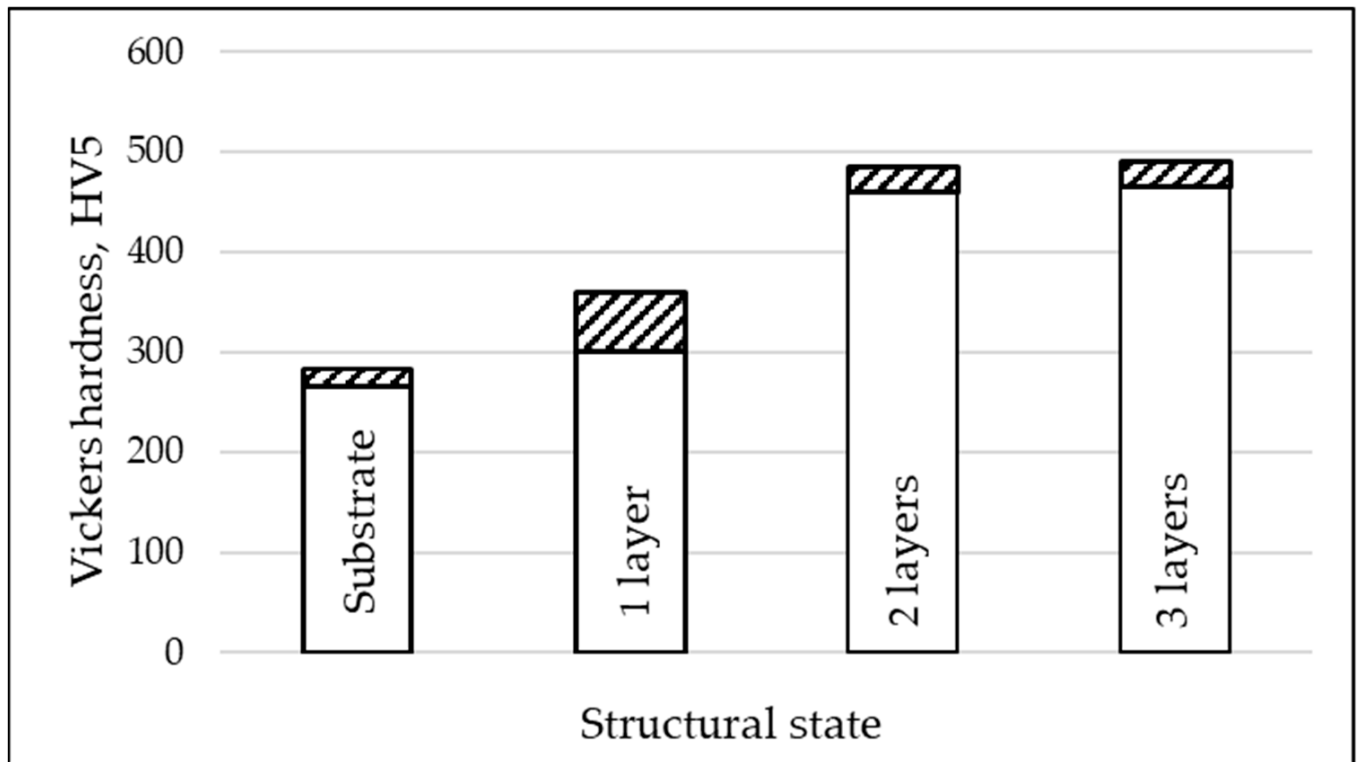


Figure 4. Histogram of the hardness values for the layer—substrate system components.

3.2. Evaluation of Cavitation Tests

In order to follow and analyze the behavior of metal alloys during cavitation attacks, specific diagrams are drawn containing the experimental values of the cumulative eroded mass M_i and of the mean erosion penetration rate v_i , as well as the variations of the mean curves $M(t)$ and $v(t)$ of these values. The relationships used have the following forms:

- for the experimental value of the cumulative eroded mass:

$$M_i = \sum_{i=1}^{i=13} \Delta m_i \text{ [mg]} \quad (1)$$

- for the analytical averaging curve of the experimental values for the cumulative eroded mass: [23,24].

$$M(t) = A \cdot t \cdot (1 - e - B \cdot t) \quad (2)$$

- for the experimental value of the mean erosion rate, related to the intermediate period:

$$v_i = \Delta m_i / \Delta t_i \text{ [mg/min]} \quad (3)$$

- for the analytical averaging curve of the experimental values obtained for the mean erosion rates [23,24].

$$v(t) = A \cdot (1 - e - B \cdot t) + A \cdot B \cdot t \cdot e - B \cdot t \quad (4)$$

where: For $i = 1$, $\Delta t_i = 0$, $M_i = 0$, where:

- i represents the number of the intermediate testing period;
- Δm_i is the mass of material lost due to erosion in period i , in g;
- Δt_i is the duration of the intermediate period “ i ” of cavitation (5, 10, and 15 min);
- A is the scale parameter, statistically established based on experimental values used to draw the approximation/mediation curve, with the condition that their deviations from it are minimal;

- B is the shape parameter of the curve, statistically established based on experimental values. The values of parameters A and B were established in the Mathcad program, version 15.0 based on a model developed in the Cavitation Erosion Research Laboratory in Timișoara [23,24]. Since cavitation is a hydrodynamic phenomenon, whose destructive effect through erosion is strongly dependent on microstructure and cavitation vibratory hydrodynamics, in the diagrams from Figure 5a–c, which express variations in cumulative masses, there is a legend with the values of the standard mean deviation intervening in the relations of the upper (S(t)) and lower (I(t)) boundaries of the dispersion domain of experimental values, known in statistics as the degree of precision or tolerance interval. For a hydrodynamic process, such as cavitation, data from the specialized literature [23,24] show that the tolerance interval values, for a correctly conducted test with rigorously controlled hydrodynamic regime parameters, can have values up to 90% (approximation error of ±10%). The relationships used to determine the standard mean deviation σ and the boundaries S(t) and I(t), according to the literature [23], adapted to the experimental data from the diagrams, have the following forms:

- for the standard mean deviation:

$$\sigma = \left[\frac{\sum_{i=0}^{13} (M_i - M(t)_i)^2}{n - 1} \right]^{\frac{1}{2}}, n = 13 \tag{5}$$

- for the tolerance range 99%:

$$S99(t) = M(t) + 1 \cdot \sigma; I99(t) = M(t) - 1 \cdot \sigma \tag{6}$$

- for the tolerance range 90%:

$$S90(t) = M(t) + 10 \cdot \sigma; I90(t) = M(t) - 10 \cdot \sigma \tag{7}$$

In Figures 5 and 6, specific diagrams of erosion caused by vibratory cavitation are presented. These include the experimental values of three samples sets, their mediation curves, and statistical values (tolerance interval, bounded by the two boundaries S and I, standard mean deviation σ), which provide data about the accuracy of conducting the experimental test.

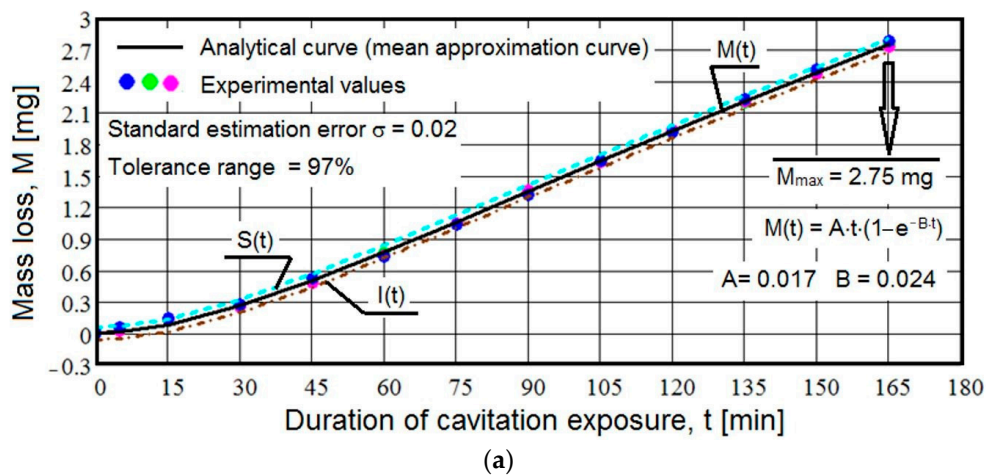
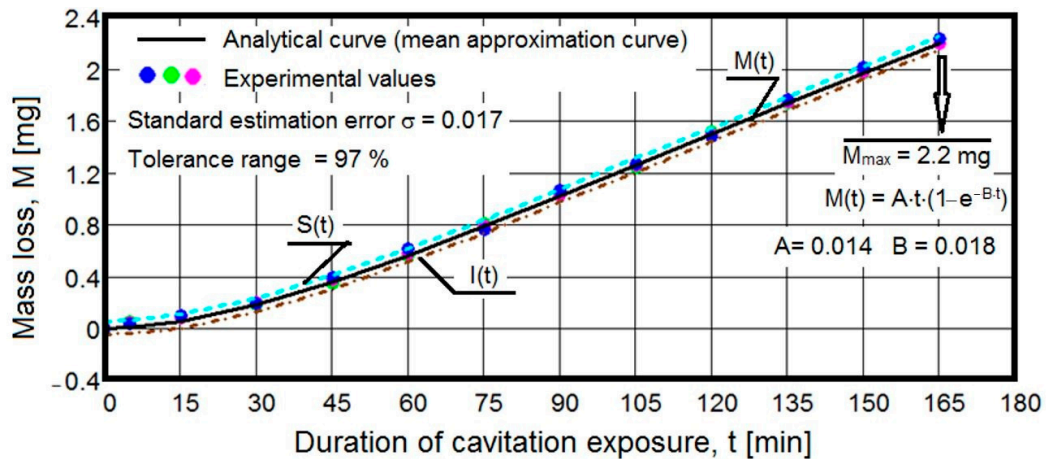
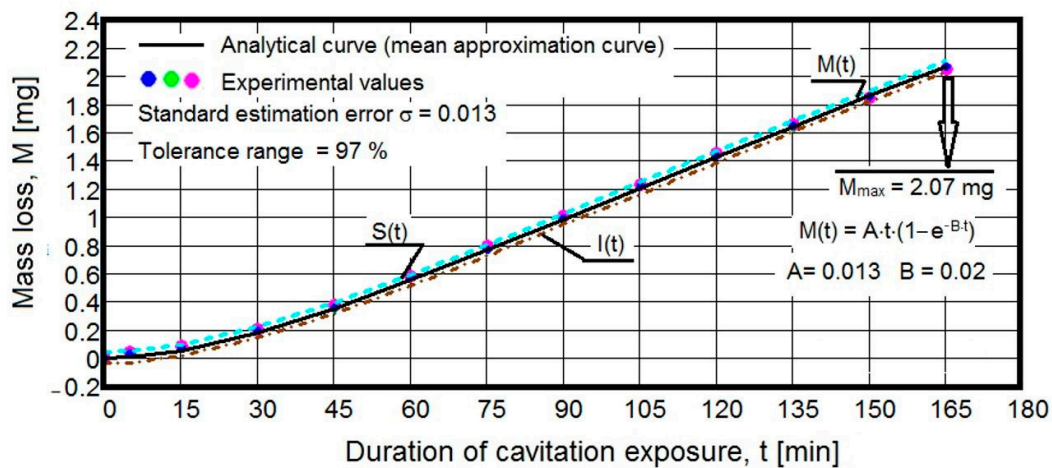


Figure 5. Cont.



(b)



(c)

Figure 5. The variation of cumulative mass losses with the duration of cavitation attack ((a)—1 deposited layer, (b)—2 deposited layers, (c)—3 deposited layers).

The data from the diagram of Figure 5, correlated with the literature [23,24], show:

- reduced differences between the maximum values of mass losses (maximum 0.13 mg—about 6%), after 165 min. of cavitation erosion;
- regardless of the hardfacing regime, the set of three samples, with one, two, and three deposited layers, exhibit similar behaviors throughout the experiment. At certain durations of cavitation, the mass losses are even identical (1 deposited layer—min. 30, 75, and 105; 2 deposited layers—min. 30, 75, and 105; 3 deposited layers—min. 75 and 135);
- a pronounced/exponential increase during the 0–60 min. of cavitation, followed by a slight decrease, resulting in the linearization of the $M(t)$ approximation curve. This behavior, according to previous studies [23,24], is dictated by the high values of hardness, homogeneously distributed within the volume of the layer structure attacked by cavitation;
- an identical and high degree of tolerance interval (97%), as well as very small values of the standard mean deviation $\sigma = (0.013–0.02)$, corresponding to the dispersion range of experimental values, confirming the accuracy of the experimental program and the consistency of the operating parameter values of the vibrating device (amplitude, frequency, water temperature, ultrasonic electronic generator power), as a result of the rigorous control provided by the software implemented in the connected computer.

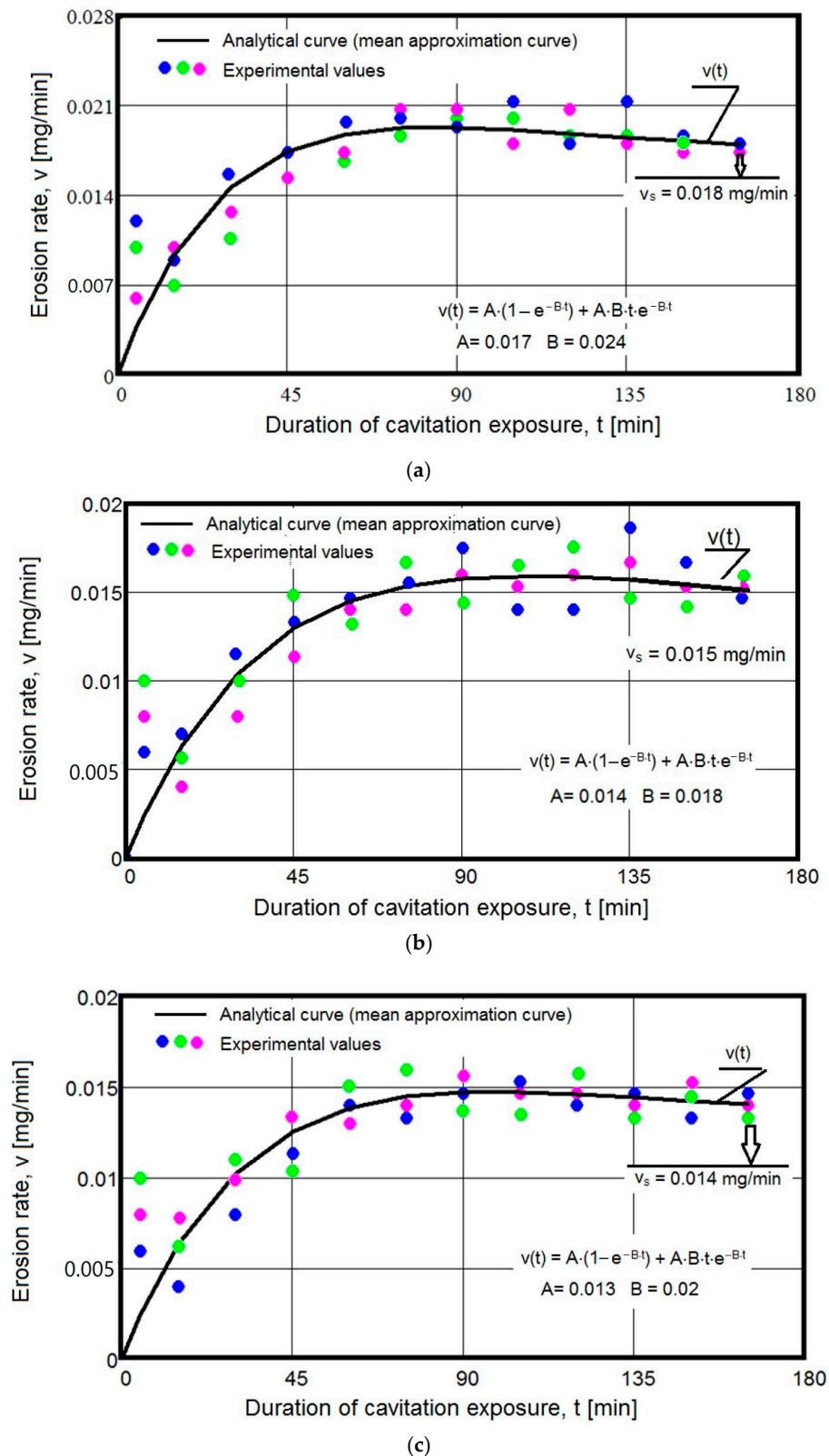


Figure 6. The variation of erosion rate with the duration of cavitation attack ((a)—1 deposited layer, (b)—2 deposited layers, (c)—3 deposited layers).

The data from the diagrams presented in Figure 6 confirm the findings from the analysis based on Figure 5 and additionally show:

- insignificant differences (up to a maximum of 0.04 mg/min) between the values of v_s , the final erosion rates, towards which the mediation curves asymptotically tend to stabilize;
- high values of erosion rates in the first 5 min, caused by the peaks of surface roughness and the abrasive dust remaining on the cavitated surface after polishing to a roughness of $R_a = \max 0.2 \mu\text{m}$. These values, according to previous experiences and literature data [23,24], do not fully represent the material loss, as cyclic stresses from microjets and cavitation shock waves during this initial period result in elastoplastic deformations and the creation of a crack network;
- the behavior of the three sets of samples, with one, two, and three deposited layers, as indicated by the dispersion of experimental values compared to mediation curves, is within the accepted errors for a dynamic process as complex as erosion generated by vibratory cavitation (see the values of the tolerance field and standard mean deviations in Figure 6);
- the evolution pattern of the mediation curve $v(t)$, reaching a maximum at 75–105 min, with an asymptotic decrease towards the stabilization value $v_s = 0.014\text{--}0.017 \text{ mg/min}$, indicates the significant effect of the coating layer hardness, which continues to harden under cyclic impacts from microjets and shock waves, as well as the attenuation of pressure peaks resulting from these impacts by the air infiltrating into the crack networks and microcavities created;
- for samples with a single deposited layer, the maximum of the $v(t)$ curve (Figure 6a) is reached earlier than for the other two samples (75 min), followed by an asymptotic decrease, indicating slightly lower resistance due to the formation of larger cavities.

The histogram from Figure 7 shows the differences between the values of the parameters MDE_{\max} (maximum value of the mean depth of erosion in the cavitated surface structure) and cavitation resistance, R_{cav} , as an expression of the hardness and microstructure effect on the surface structure resistance to the stresses of cavitation shock waves and microjets.

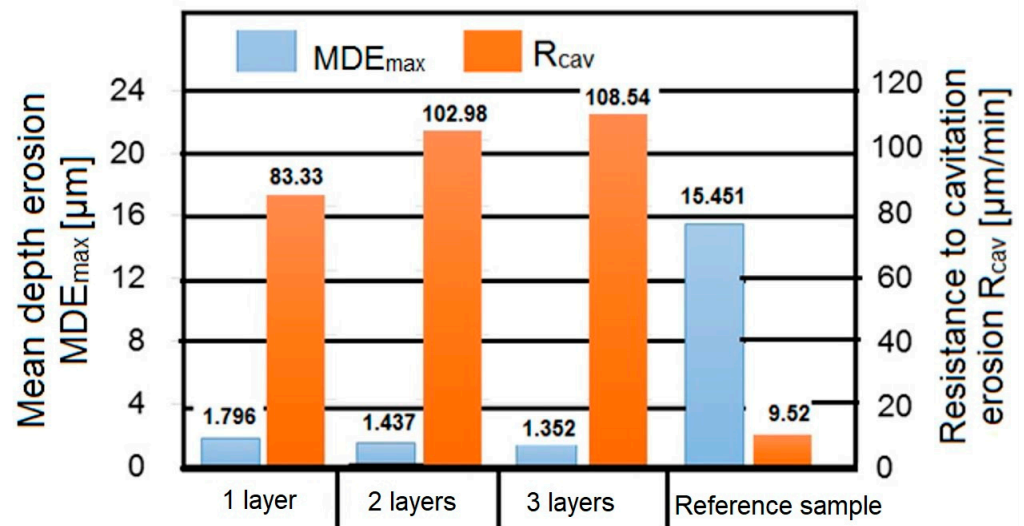


Figure 7. Histogram showing the comparison of cavitation erosion resistance.

It is noted that the parameters MDE_{\max} and R_{cav} , as indicated by ASTM G32-2016 [22], are determined using the relationships used in the practice of our laboratory [23,24]:

$$MDE_{\max} = \frac{4 \cdot M_{\max}}{\rho \cdot \pi \cdot d_p^2} \quad [\mu\text{m}] \quad (8)$$

$$R_{\text{cav}} = \frac{\rho \cdot \pi \cdot d_p^2}{4 \cdot v_s} \quad [\text{min}/\mu\text{m}] \quad (9)$$

where:

M_{max} —cumulative mass (Figure 5);

ρ —steel density, (7810 kg/m³);

d_p —the diameter of the sample surface subjected to cavitation attack ($d_p = 15.8$ mm);

v_s —The rate value towards which the $v(t)$ curve asymptotically tends (final value Figure 6).

From the histogram presented in Figure 7, the following conclusions can be drawn:

- by depositing 2–3 layers of austenitic manganese alloy, the cavitation erosion resistance is significantly higher than that of the Duplex stainless steel structure resulting from the solution heat treatment (reference sample).
- according to the values of the two parameters, the resistance of the deposited layers to cavitation microjet stresses increases compared to that of the solution heat-treated stainless steel by a factor ranging from 8.6 to 11.4, regardless of the parameter considered, MDE_{max} or R_{cav} .
- among the three deposited layers, the highest resistance is obtained for layer 2 and 3; the difference in their resistances is insignificant (approximately 6% after MDE_{max} and approximately 5.4% after R_{cav} —practically within the accepted error margin for cavitation erosion mechanics [23,24]).
- the increase in cavitation resistance achieved by surfaces with two and three deposited layers compared to that of surfaces with a single deposited layer is between 23% and 30%.

3.3. Microstructural Examinations on the Coating-Substrate System

Figure 8 shows the micrographic image of a cross-section through the deposited metal-base metal system by deposition of a single layer. Due to the complete melting of the filler material and a thin portion of the base metal, the weld pool is formed. The process of primary crystallization of the molten metal pool ensures a metallurgical bond between the two materials, and discontinuities in the metal continuity (such as pores, blowholes, shrinkage voids, and cracks) are absent. In the lower zone of the deposited metal layer (towards the base metal), a dendritic microstructure oriented in the direction of the thermal gradient is formed. Since the cooling rate from the peak temperature reached during welding is high, the growth of crystalline grains in the molten zone occurs from pre-existing grains, a process referred to as epitaxial growth.

By pulsed current welding, the heat input into the workpieces is lower than in conventional arc welding, and the cooling rate is higher. The calculation relationship for linear energy input in welding is:

$$E_l = \frac{U_a \times I_s}{V_s} \times 60 [\text{J}/\text{cm}] \quad (10)$$

where:

U_a —electric arc voltage, V;

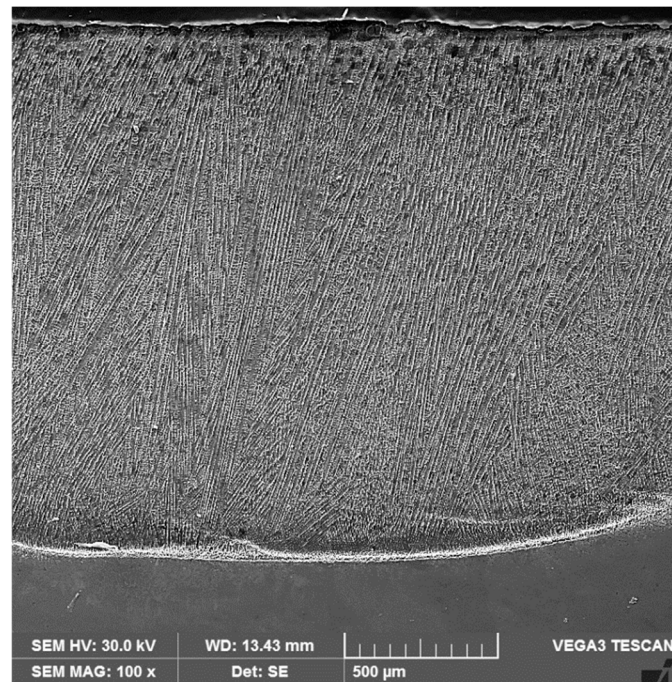
I_s —welding current, A;

v_s —welding speed, cm/min.

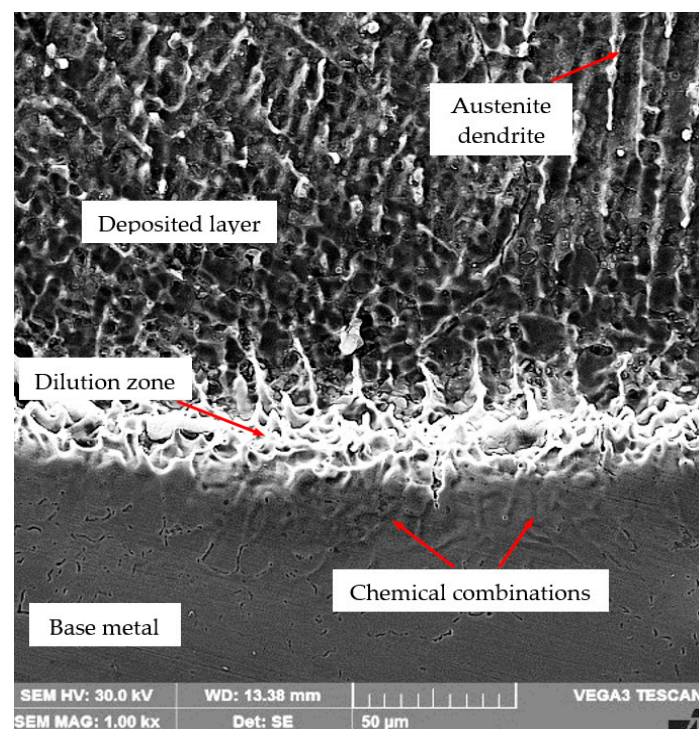
Throughout the welding process, the temperature between two successive passes has been maintained at 150–200 °C to avoid the precipitation temperatures of brittle phases such as sigma (σ), chi (χ), and alpha-prime (α'). This occurs when Duplex stainless steels are subjected to temperatures of 300–1000 °C. This phenomenon is practically inevitable because during the hardfacing through welding, the substrate surface undergoes melting. Therefore, even if most of the material remains below 300 °C, there is always a zone where temperatures will fall within the embrittlement range, even if only for a short period.

Figures 9 and 10 present the results of energy dispersive X-ray analyses conducted on both the first deposited layer and the last deposited layer. Comparing the concentration

values of Fe, Cr, Ni, Mn, and Mo in the first deposited layer (Figure 9) with those specific to the reference metal and those present in the last deposited layer (Figure 10) confirms the existence of dilution phenomenon between the two components of the system.

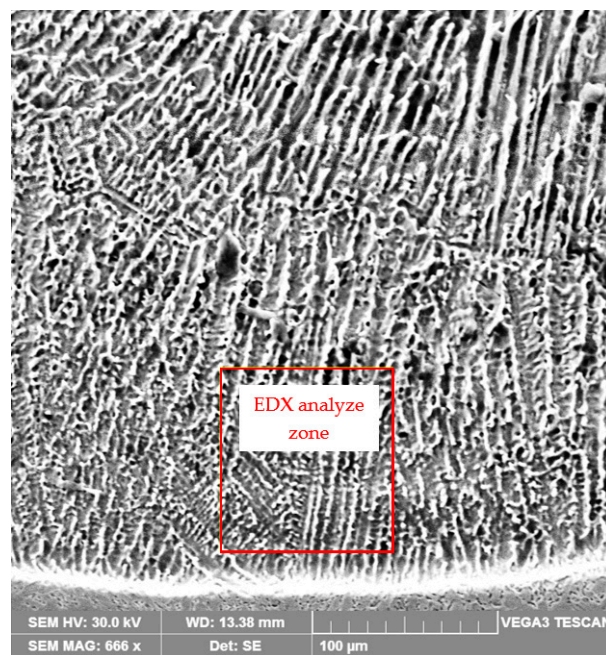


(a)

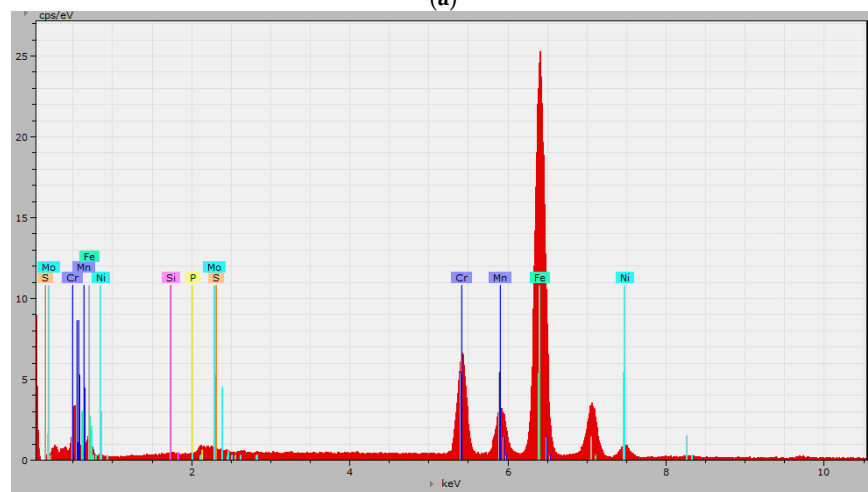


(b)

Figure 8. SEM microstructural image of a cross-section through the coating-substrate system: (a) $\times 100$ magnification; (b) $\times 1000$ magnification.



(a)

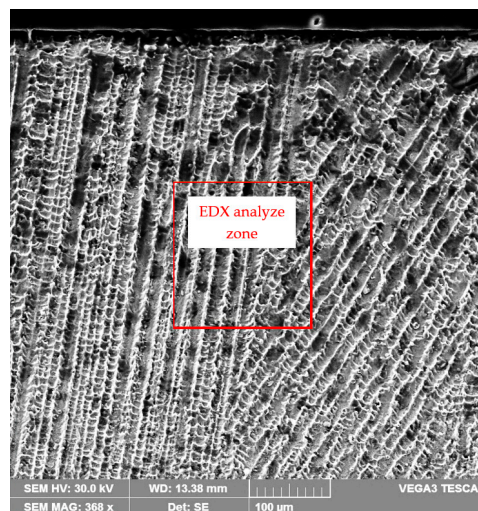


(b)

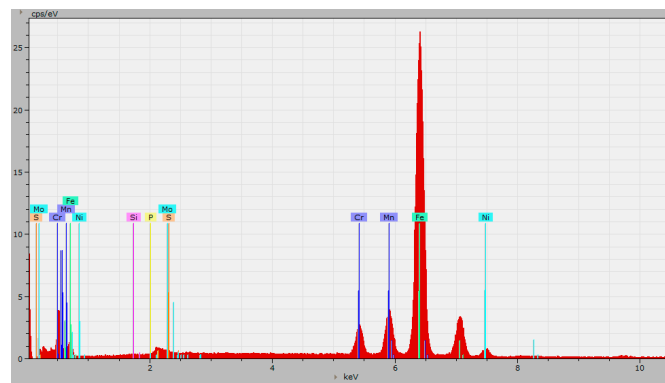
Element	Series	Mass C. (wt.%)	Norm. C. (wt.%)	Atom C. (at.%)	Error (1 Sigma) (wt.%)
Ni	K series	3.49	3.58	3.39	0.13
Cr	K series	10.75	11.03	11.79	0.32
Mn	K series	6.12	6.28	6.36	0.20
Si	K series	0.31	0.31	0.62	0.05
P	K series	0.09	0.09	0.16	0.04
S	K series	0.03	0.03	0.05	0.02
Fe	K series	75.04	76.96	76.63	1.93
Mo	K series	1.67	1.71	0.99	0.22
	Total	97.50	100.00	100.00	

(c)

Figure 9. SEM microstructural image (a), dispersion spectrum (b), and chemical composition (c) of the first deposited layer.



(a)



(b)

Element	Series	Mass C. (wt.%)	Norm. C. (wt.%)	Atom C. (at.%)	Error (1 Sigma) (wt.%)
Ni	K series	2.63	2.87	2.71	0.11
Cr	K series	4.03	4.39	4.68	0.14
Mn	K series	13.59	14.35	14.44	0.26
Si	K series	0.33	0.36	0.71	0.05
P	K series	0.09	0.09	0.15	0.03
S	K series	0.02	0.02	0.05	0.01
Fe	K series	71.02	77.74	77.16	1.96
Mo	K series	0.16	0.17	0.10	0.08
	Total	91.87	100.00	100.00	

(c)

Figure 10. SEM microstructural image (a), dispersion spectrum (b), and chemical composition (c) of the last deposited layer.

3.4. Surface Topography of the Cavitated Surfaces

The topographic images of the samples' surfaces taken from the base material and from those hardened by depositing the three layers, which were tested for cavitation erosion for 165 min, are shown in Figure 11. Microscopic examinations highlight the formation of craters with depths greater than 18 μm (Figure 11a), determined by the preferential cavities of the ferrite and the grain boundary separation limits, which are more fragile. It is emphasized that the separation limits between the two phases α/γ and those between the crystalline grains of these phases are less capable of absorbing the deformation energy due to the stresses induced in the material by the impact waves of cavitation, and as a result, they erode more rapidly than the γ solid solution microstructure. On the other hand, on

surfaces hardened by depositing the three layers (Figure 11b), it is observed that cavitation depths do not exceed 6 μm , and degradation is slower and more uniform.

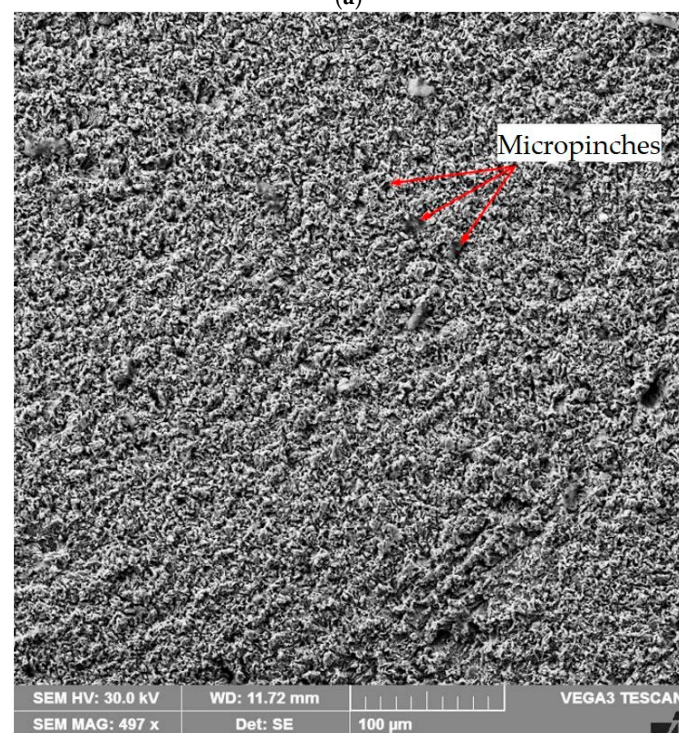
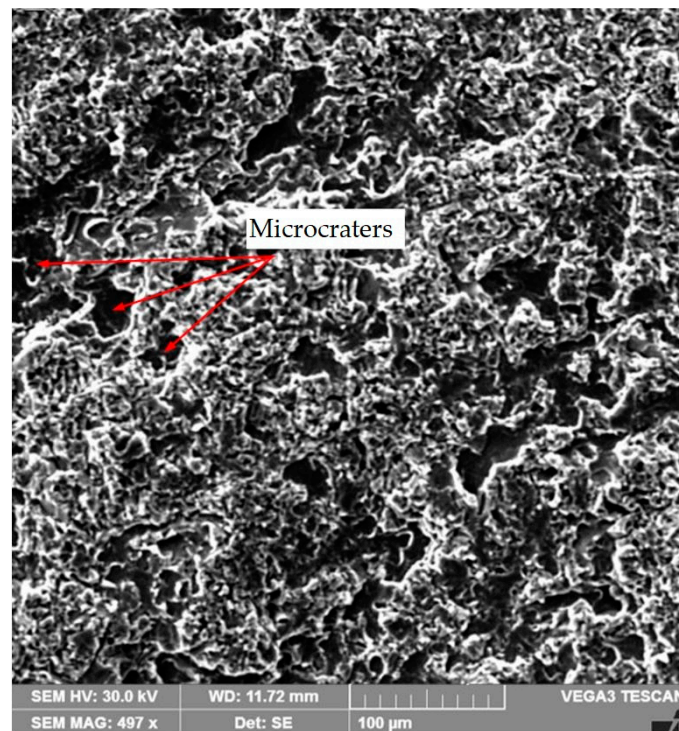


Figure 11. Topography (SEM image) of the surfaces tested for cavitation for 165 min: (a)—base metal; (b)—hardened layer.

4. Conclusions

The hardfacing process by welding of the Duplex stainless steel components surface, using austenitic manganese alloy electrodes such as “Citomangan”, promotes a significant

improvement in cavitation erosion resistance. According to the reference parameter values (M_{\max} , vs , MDE_{\max} , or R_{cav}), the highest resistance to cyclic cavitation vibrations is found in surfaces with two or three deposited layers.

The lower cavitation resistance of surfaces with a single deposited layer is explained by the dilution phenomenon of the layer with the substrate, which is specific to any welding deposition process.

Compared to the substrate material, the increase in cavitation erosion resistance provided by the hardfacing by welding process is very high, exceeding eight times. The main mechanical property that has determined this increase is surface hardness, reaching values of 465–490 HV5 due to the high mechanical work hardening capacity of the austenitic manganese alloys.

Author Contributions: Conceptualization, I.M. and I.B.; methodology, I.M., D.M., I.-D.U., C.M.C. and I.B.; investigation, I.M., D.M., I.-D.U., C.M.C. and I.B.; writing—original draft preparation, I.M., I.-D.U. and I.B.; writing—review and editing, I.M., C.M.C., I.-D.U. and I.B.; visualization, I.M., D.M., I.-D.U., C.M.C. and I.B.; supervision, I.M. and I.B.; project administration, I.M. and I.B.; funding acquisition, C.M.C. All authors have read and agreed to the published version of the manuscript.

Funding: This project is supported by a grant from the Romanian Ministry of Education and Research, CNCS–UEFISCDI, project number PN-IV-P1-PCE-2023-1425.

Data Availability Statement: Not applicable.

Acknowledgments: This project is supported by a grant from the Romanian Ministry of Education and Research, CNCS–UEFISCDI, project number PN-IV-P1-PCE-2023-1425.

Conflicts of Interest: The authors declare no conflicts of interest.

References

- Whitesides, R.W. *Interesting Facts (and Myths) about Cavitation*; PDHonline: Fairfax, VA, USA, 2012; Volume 225.
- Zhao, J.; Ning, L.; Zhu, J.; Li, Y. Investigation on Ultrasonic Cavitation Erosion of Aluminum–Titanium Alloys in Sodium Chloride Solution. *Crystals* **2021**, *11*, 1299. [[CrossRef](#)]
- Carlton, J. *Marine Propellers and Propulsion*, 2nd ed.; Carlton, J., Ed.; Chapter Cavitation; Butterworth-Heinemann: Oxford, UK, 2012; pp. 209–250.
- Ghose, J.P.; Gokarn, R.P. *Basic Ship Propulsion*; Chapter Propeller Materials; Allied Publishers: Kharagpur, India, 2004; pp. 166–173.
- Fitch, E.C. Machinery Lubrication. Chapter Cavitation Wear in Hydraulic Systems. 2011. Available online: <http://www.machinerylubrication.com/Articles/Print/380> (accessed on 10 January 2024).
- Escaler, X.; Egusquiza, E.; Farhat, M.; Avellan, F.; Coussirat, M. Detection of cavitation in hydraulic turbines. *Mech. Syst. Signal Process.* **2006**, *20*, 983–1007. [[CrossRef](#)]
- He, Z.; Qin, Z.; Gao, Z.; Wu, Z.; Hu, W. Synergistic effect between cavitation erosion and corrosion of Monel K500 alloy in 3.5 wt% NaCl solution. *Mater. Charact.* **2023**, *205*, 113340. [[CrossRef](#)]
- Zhao, T.; Wang, L.; Zhang, S.; Zhang, C.H.; Sun, X.Y.; Chen, H.T.; Bai, X.L.; Wu, C.L. Effect of synergistic cavitation erosion-corrosion on cavitation damage of CoCrFeNiMn high entropy alloy layer by laser cladding. *Surf. Coat. Technol.* **2023**, *472*, 129940. [[CrossRef](#)]
- Wang, L.; Mao, J.; Xue, C.; Ge, H.; Dong, G.; Zhang, Q.; Yao, J. Cavitation-Erosion behavior of laser clad Low-Carbon Cobalt-Based alloys on 17-4PH stainless steel. *Opt. Laser Technol.* **2023**, *158*, 108761. [[CrossRef](#)]
- Zhao, T.; Zhang, S.; Wang, Z.Y.; Zhang, C.H.; Zhang, D.X.; Wang, N.W.; Wu, C.L. Cavitation erosion/corrosion synergy and wear behaviors of nickel-based alloy coatings on 304 stainless steel prepared by cold metal transfer. *Wear* **2022**, *510*, 204510. [[CrossRef](#)]
- Wang, Y.; Hao, E.; Zhao, X.; Xue, Y.; An, Y.; Zhou, H. Effect of microstructure evolution of Ti6Al4V alloy on its cavitation erosion and corrosion resistance in artificial seawater. *J. Mater. Sci. Technol.* **2022**, *100*, 169–181. [[CrossRef](#)]
- Chen, F.; Du, J.; Zhou, S. Cavitation erosion behaviour of incoloy alloy 865 in NaCl solution using ultrasonic vibration. *J. Alloys Compd.* **2022**, *831*, 154783. [[CrossRef](#)]
- Karimi, A.; Karimipour, A.; Akbari, M.; Razzaghi, M.M.; Ghahderijani, M.J. Investigating the mechanical properties and fusion zone microstructure of dissimilar laser weld joint of duplex 2205 stainless steel and A516 carbon steel. *Opt. Laser Technol.* **2023**, *158*, 108875. [[CrossRef](#)]
- Kwok, C.T.; Man, H.C.; Cheng, F.T. Cavitation erosion of duplex and super duplex stainless steels. *Scr. Mater.* **1998**, *39*, 1229–1236. [[CrossRef](#)]
- Karimi, A. Cavitation erosion of a duplex stainless steel. *Mater. Sci. Eng.* **1987**, *86*, 191–203. [[CrossRef](#)]
- Al-Hashem, A.; Riad, W. The effect of duplex stainless steel microstructure on its cavitation morphology in seawater. *Mater. Charact.* **2001**, *47*, 389–395. [[CrossRef](#)]

17. Wu, Y.; Lian, Y.; Li, Y.; Feng, M. Cavitation Erosion Behavior of 2205 and 2507 Duplex Stainless Steels in Distilled Water and Artificial Seawater. *Tribol. Online* **2023**, *18*, 482–493. [[CrossRef](#)]
18. Lakshmi Prasanna, G.; Tanya, B.; Subbiah, R.; Vinod Kumar, V. Effect of nitriding on duplex stainless steel—A review. *Mater. Today Proc.* **2020**, *26*, 950–955. [[CrossRef](#)]
19. Garzón, C.M.; Thomas, H.; Francisco dos Santos, J.; Tschiptschin, A.P. Cavitation erosion resistance of a high temperature gas nitrided duplex stainless steel in substitute ocean water. *Wear* **2005**, *259*, 145–153. [[CrossRef](#)]
20. Escobar, J.D.; Velásquez, E.; Santos, T.F.A.; Ramirez, A.J.; López, D. Improvement of cavitation erosion resistance of a duplex stainless steel through friction stir processing (FSP). *Wear* **2013**, *297*, 998–1005. [[CrossRef](#)]
21. Kwok, C.T.; Lo, K.H.; Chan, W.K.; Cheng, F.T.; Man, H.C. Effect of laser surface melting on intergranular corrosion behaviour of aged austenitic and duplex stainless steels. *Corros. Sci.* **2011**, *53*, 1581–1591. [[CrossRef](#)]
22. *Standard G32; Standard Method of Vibratory Cavitation Erosion Test*. ASTM: West Conshohocken, PA, USA, 2016.
23. Bordeasu, I. *Monografia Laboratorului de Cercetare a Eroziunii prin Cavitatie al Universitatii Politehnica Timisoara, 1960–2020*; Editura Politehnica: Timișoara, Romania, 2020.
24. Bordeasu, I.; Patrascioiu, C.; Badarau, R.; Sucitu, L.; Popoviciu, M.; Balasoiu, V. New contributions in cavitation erosion curves modeling. *FME Trans.* **2006**, *34*, 39–44.

Disclaimer/Publisher’s Note: The statements, opinions and data contained in all publications are solely those of the individual author(s) and contributor(s) and not of MDPI and/or the editor(s). MDPI and/or the editor(s) disclaim responsibility for any injury to people or property resulting from any ideas, methods, instructions or products referred to in the content.